Detailed theoretical photoelectron angular distributions for LiF(100)

Eric L. Shirley
National Institute of Standards and Technology, Physics Laboratory, Radiometric Physics Division, Gaithersburg, Maryland 20899

Louis J. Terminello and John E. Klepeis
Lawrence Livermore National Laboratory, P. O. Box 808, Livermore, California 94551

Franz J. Himpsel
IBM Thomas J. Watson Research Center, Yorktown Heights, New York 10598

(Received 31 July 1995)

We model photoelectron angular distributions obtained earlier by Himpsel *et al.* [Phys. Rev. Lett. **68**, 3611 (1992)] for the F 2*p* bands in LiF(100). The F 2*p* states are treated within a many-body, quasiparticle approach, and a nearly-free-electron model is presented for the description of conduction-band states relevant to the photoemission process. In the quasiparticle results, we find a band gap of 14.4 eV and a F 2*p* bandwidth of 3.6 eV, in satisfactory agreement with experimental values of 14.2 and 3.5 eV for these respective quantities. A method for computing photoelectron angular distributions is presented, followed by a comparison of simulated and measured photoelectron angular distributions for several parts of the three-dimensional Brillouin zone. In this comparison, constant-energy contours in the F 2*p* bands are clearly portrayed in both theoretical and experimental images. Using the model, we also identify the origin of a Brillouin-zone-dependent intensity variation for equivalent valence states, i.e., states which are related by reflection through a (010)-type Bragg plane and which lie close to such a plane.

I. INTRODUCTION

Lithium fluoride (LiF) has been widely used in several technological applications such as in x-ray monochromators,[1] as a filter for ultraviolet radiation,[2] and in thermoluminescent dosimetry.[3] LiF may also prove useful in germanium-device, epitaxial heterostructures,[4] and has been considered for neutron detector[5] and other uses.[6] LiF is also interesting for a variety of fundamental physical reasons, such as the fact that it lies essentially at one extreme of the ''band-gap scale,'' making it a prototypical insulator. Indeed, in many ways, this rock-salt-structure material may be thought of as a face-centered-cubic, noble-gas solid.

Among the many intriguing physical properties of this material, LiF has the widest band gap (14.2 eV) of any material except for exotic systems such as noble-gas solids. Along with its large band gap, LiF exhibits strong excitonic effects in its optical spectra.[7–9] These effects, interesting in their own right, considerably complicate the determination of the mobility edge (quasiparticle band gap) using optical spectroscopy.[8] One may also consider the problems of understanding and measuring the F 2*s* and F 2*p* bandwidths.[10,11] There are substantial contributions to these parameters from many-body effects. Indeed, the F 2*p* band has been proposed as a good system for studying the behavior of localized electron states (in this case, F 2*p* states) in solids.[10]

Angle-resolved photoelectron spectroscopy, both in its direct and inverse versions, is an invaluable probe for use in studying band structures of solids. In this work, we model a variety of experimental data for LiF, and especially valence-band photoelectron spectroscopy results. We first model the band structure of this material, including the band gap,[12] F 2*p* band width,[10] and F 2*s* to F 2*p* energy separation.[13] This is done in a detailed, many-body (quasiparticle) fashion, following the approach of Hybertsen and Louie.[14] Using their approach, we find good agreement with experiment for the above quantities.

Once the band-structure results are in hand, we utilize them to simulate detailed photoelectron angular distributions (PAD's) for LiF. Such PAD's for LiF F 2*p* electrons were measured[10] using a display-type electron analyzer with an 84° full-cone angle of acceptance.[15] Because data for each PAD were collected using monochromatic incident radiation, while counting only the photoelectrons lying within a narrow range of energies, the PAD's displayed reciprocal-space, constant energy contours in the LiF, F 2*p* band structure. This enabled unambiguous determination of the F 2*p* band extrema, yielding a definitive measurement of the bandwidth, along with the dispersion of these F 2*p* states. Other examples of rendering band structures, and particularly Fermi surfaces, as two-dimensional slices in *k* space have been reported recently.[16]

The present PAD's contain much more information regarding the F 2*p* valence-band states than was used to determine the bandwidth. However, a great deal of this information is very complicated to interpret. The PAD's sample three F 2*p* bands that disperse in a complicated fashion as one traverses the Brillouin zone. Rather than attempt to infer more about the band structure from the experimental PAD's we found it more profitable to compare the theoretical PAD's with their experimental counterparts. Besides ascertaining the trustworthiness of the theory, such comparisons may also distinguish information in the experimental PAD's that is related to the intrinsic, F 2*p* bands, versus all forms of extrinsic, experimental artifacts.

This paper is organized as follows. We first define the

''quasiparticle'' description of electrons that we use. Then, a section is devoted to the electronic structure of bulk LiF; electronic excitations in LiF have been studied extensively both experimentally and theoretically and we review some of the work by others. Particular care must be taken, we note, when inferring band edges from absorption spectra. We present quasiparticle calculations, carried out by the Hybertsen-Louie method, of the LiF band structure. With the results of these calculations, we construct Slater-Koster[17] and nearly-free-electron descriptions of photoelectron initial and final states, respectively.

The theory of photoemission from solids is well developed and has been described in several classic papers.[18–20] Building on this work, we develop the particular model that is used here to compute PAD's. A PAD is identified by photon energy and polarization and by the electron initial-state energy E. We use the convention of having $E=0$ for states at the valence-band maximum. Several pertinent issues are addressed here: kinematical effects, surface effects (since we describe electron states based largely on calculations for bulk LiF), and various experimental considerations. We discuss the elements of the present model and we assemble them to arrive at formulas used here to predict PAD's.

The central result of this work, simulated PAD's are presented and compared to their experimental counterparts. The comparison includes quantitative determination of the level of correlation between simulation and experiment. The PAD's are displayed in this work using gray-scale images, a manner of presentation that reveals physical effects quite readily. We analyze one particularly striking effect seen in the images, viz., a ''zone-selection'' effect. This involves a lowering of the symmetry, which s to be found in the PAD's, from the symmetry that is present in the underlying band structure. (This symmetry in the band structure is best illustrated within the extended-zone scheme. A different sort of zone-selection effect has been reported elsewhere for graphite.[21]) Thereafter, we provide some concluding remarks.

II. QUASIPARTICLE CONCEPT

One can discuss photoemission within a *quasiparticle* picture.[22] In such a picture, the photoemission process, which involves photoexcitation of a complex, many-electron system (a crystal), is treated phenomenologically as the excitation of a single, renormalized electron (quasiparticle). A quasiparticle treatment of electrons can be based on the rigorous, field-theoretic modeling of a many-body system. The band-structure calculation in this work relies on a detailed, field-theoretic treatment of electron self-energy effects.[14] In modeling PAD's meanwhile, we rely on more approximate (intuitive and computationally simpler) quasiparticle descriptions of electrons. A treatment of the PAD's at the same level of detail as that used to describe the valence band structure would be very difficult.

A *quasiparticle energy* is either (i) minus the removal energy for an occupied state or (ii) the addition energy for an unoccupied state. Quasiparticle energies, for states in valence and conduction bands, can be measured respectively by direct and inverse photoelectron spectroscopy. These methods respectively involve processes in which a solid loses or acquires an electron. Such energies are not directly probed by nonionizing excitations that are probed, for instance, in absorption spectroscopy. Such a spectroscopy really involves the creation of electron-hole pairs, but not single electrons or holes. In particular, the onset of absorption, as one increases incident photon energy, occurs initially because of the formation of excitons.

When computing photoelectron angular distributions, one needs to properly identify the initial and final states of one's physical system. In the case of photoemission from a solid, the initial state of the system is a crystal in its ground state, plus an incoming photon. The final state of the system, achieved by photoexcitation when that photon is absorbed, is the crystal with a hole in its valence band, plus the ejected photoelectron. One may describe initial and final states during photoemission not only in terms of the system initial and final states, but more relevantly for this work, also in terms of the electron (quasiparticle) initial and final states.

In this work, photoexcitation matrix elements between system initial and final states are approximated by one-electron matrix elements between associated, quasiparticle wave functions. Whereas photoemission involves an ionizing excitation, there are nonetheless electron-hole interactions in the system final state and we neglect these interactions. Within the quasiparticle approach, necessary summations over electron initial and final states are achieved by direct summation over initial states and by construction of an electron final-state propagator. In photoemission, the system final state (for the many-body solid) can be a superposition of a continuum of stationary states. Phenomenologically, this leads to finite mean free paths for photoelectrons. In a quasiparticle description, quasiparticles correspondingly have complex self-energies (which produces equivalent damping).

III. ELECTRONIC STRUCTURE OF BULK LiF

A. Background: Previous work

As determined from photoelectron spectroscopy, the band gap of LiF is 14.1–14.2 eV,[12] separating F $2p$ valence and Li $2s$ conduction bands. The conduction-band minimum (CBM) is at the zone center (Γ). The valence-band maximum (VBM) is also at the zone center, and F $2p$ band energies extend over a total width of 3.5 eV.[10] The next lowest occupied band has predominantly F $2s$ character and its center is found to lie 24.9 eV below the VBM.[13]

Besides photoelectron spectroscopy, which gives the above results, one may also consider optical data.[7–9] Consider ϵ_2 spectra presented in these references, where $\epsilon_2(\omega)$ is the imaginary part of the dielectric function as a function of photon frequency ω. These spectra exhibit a broad excitonic peak near photon energy $\hbar\omega=12.6$ eV, followed by a shoulder beginning around $\hbar\omega=13.7$ eV, where $\epsilon_2(\omega)$ has a local minimum. (In early work, this minimum was incorrectly interpreted as the mobility edge.) Going to even higher photon energies, $\epsilon_2(\omega)$ varies smoothly until above $\hbar\omega=16$ eV. There is no particular indication of the mobility edge near $\hbar\omega=14.2$ eV in $\epsilon_2(\omega)$, illustrating the difficulty of directly assessing such a quantity by optical methods. For instance, by analyzing reflectance data with the aid of a particular model for excitons, Piacentini[9] estimates the mobility edge to lie at 14.5 eV, slightly higher than is given by photoemission.

Of the past theoretical work on the band structure of LiF, we shall emphasize a density-functional[23] calculation by Zunger and Freeman,[24] done using the $X\alpha$-method with several values of α, and a Hartree-Fock calculation by Kunz,[25] who also cites other work. As is common in density-functional theory, Zunger and Freeman find too small a gap: 9.8 eV for $\alpha=\frac{2}{3}$ and 10.5 eV for $\alpha=1$. However, the F $2p$ bandwidth is about 3.1 eV for $\alpha=\frac{2}{3}$, and it is even smaller (2.5 eV) for $\alpha=1$. Zunger and Freeman also present a model that considers the total-energy difference induced by introduction of an electron or hole in the solid. This leads to a 13.9-eV band gap, but Zunger and Freeman do not discuss the F $2p$ bandwidth found in this approach. As is common in Hartree-Fock results, the band gap is far too large (22.7 eV) in Kunz's work. With the aid of a particular model for correlation effects, Kunz estimates correlation effects on band energies. This gives a band gap much closer to the experimental one. Kunz found a width of the F $2p$ bands equal to 4 eV without correlation effects, but 3.1 eV with correlation effects.

B. This work: Computational details

We calculate band energies in the Hybertsen-Louie scheme, which is an *ab initio*, many-body, quasiparticle approach. We rely on the "*GW* approximation" to the one-electron, self-energy operator. This approximation involves expansion of the electron self-energy in terms of the Green's function G and a dynamically screened Coulomb interaction W. For solids, which have substantial screening effects, terminating the expansion at lowest order in W is often an acceptable approximation, known as the *GW* approximation. This approximation treats many-body effects on band energies with greater accuracy than is found in either the density-functional or Hartree-Fock approaches, even *modulo* the above-mentioned *ad hoc* extensions of such approaches. The *GW* approximation has typical errors of 0.1–0.2 eV in band-energy differences for a wide variety of semiconductors and insulators, but it is computationally more demanding. For an extensive discussion of the *GW* approach, we refer the reader to the length review by Hedin and Lundqvist.[22] A detailed presentation of more recent, first-principles quasiparticle calculations is given in the work by Hybertsen and Louie,[14] in addition to others.[26,27]

In computing the band structure, we rely on first principles, except for the use of the experimental (zero-temperature, zero-pressure) lattice constant (4.03 Å) and crystal structure (rock salt).[28] Our work includes a self-consistent calculation of the charge density and band orbitals and energies in the local-density approximation (LDA).[23] We use the Ceperley-Alder exchange-correlation functional,[29] but generate standard, norm-conserving pseudopotentials[30] by the methods of Vanderbilt[31] in the core-polarization-potential (CPP) formulation.[27,32–34] This formulation treats core-valence exchange interactions in an (exact) Hartree-Fock fashion and provides a model for core-valence correlation, including dynamical core polarization in the presence of valence electrons. We employ an extended version of the CPP approach of Müller, Flesch, and Meyer,[33] with first-principles CPP parameters of Shirley and Martin.[32] (In contrast, Shirley, Zhu, and Louie[27] employed CPP's parametrized using vapor-phase, atomic spectral data for several elements present in semiconductors, because of difficulties with accurately treating core-valence correlation strictly by first principles in post-transition elements.)

The solid-state, LDA calculation was done using separable pseudopotentials.[35] Pseudopotential d channels were considered as local potentials and nine radial projectors described s- and p-channel nonlocality. The nine projectors constrained the nonlocal (separable) pseudopotentials to have the same action as semilocal (nonseparable) pseudopotentials within the subspace of the zeroth, first, and second energy derivatives of the radial pseudovalence wave functions. We carried out rigorous tests to ensure the absence of spurious solutions in the separable case. The radial Schrödinger equation was solved for the solution regular at the origin, but with arbitrary boundary conditions at a radius well outside of the atomic core. This solution was obtained by three different approaches: (i) radial integration of the ordinary differential equation in the semilocal case; (ii) taking the effective Hamiltonian associated with each set of imposed boundary conditions and solving it for the lowest few energies using a converged, finite basis set, for the semilocal pseudopotential; and (iii) the same as (ii), but for the separable pseudopotential. For the entire range of energies probed by summing over bands to construct the solid-state, one-electron Green's function, there were only minor differences between scattering properties found in all three approaches.

We used a plane-wave basis set with a 100-Rydberg cutoff and ten $\mathbf{k}$ points[36] in the irreducible wedge of the Brillouin zone. Hamiltonian-matrix *diagonalization* was done essentially in the preconditioned, conjugate-gradient fashion discussed by Teter, Payne, and Allan.[37] (A minor difference was our exact diagonalization of a small block of the matrix to enhance preconditioning. This was actually of little benefit.) We achieved self-consistency in the indirect Broyden scheme.[38] To accelerate iterative diagonalization, we used wave functions from previous iterations as initial guesses for wave functions in each self-consistency loop, beginning with random numbers in the first iteration. Fast Fourier-transform (FFT) technology was used extensively.

We included the lowest 60 bands in the Green's function used in quasiparticle calculations, which included all states up to 130 eV above the electron chemical potential. FFT techniques were used in convolutions required to compute the static Linhard polarizability matrix and self-energy. Bare and screened Coulomb potentials were expanded up to 100-Rydberg and 36-Rydberg cutoffs, respectively. All local-field effects were included. The dielectric matrix was extended to finite frequency using a generalized, plasmon-pole model, suitably modified according to the CPP formulation.[27] We obtained, theoretically, $\epsilon_\infty=1.97$, in adequate agreement with the experimental value of 1.94.[39]

C. This work: Band-structure results

Besides the quasiparticle calculations, we also carried out LDA calculations with LDA-based pseudopotentials, for diagnostic purposes. These LDA-based pseudopotentials were generated in exactly the same fashion as the CPP-based pseudopotentials used throughout the quasiparticle calculations, except for treatment of core-valence exchange and correlation. When generating the LDA-based pseudopotentials,

TABLE I. Band gap, F $2s$ to F $2p$ interval, and F $2p$ bandwidth in LiF, as found by various approaches discussed in the text. All energies are in eV.

Approach	Band gap	F $2s$–F $2p$ interval	F $2p$ bandwidth
Experiment			
photoemission	14.1(1)[a]	24.9[b]	3.5[c]
optical data	14.2(2),[d] 14.5[e]		
Theory			
this work (quasiparticle)	14.4	21.7	3.6
this work (LDA)	8.7	19.0	3.1
$X\alpha, \alpha=\frac{2}{3}$[f]	9.8	≈20	3.1
$X\alpha, \alpha=1$[f]	10.5	≈20	2.3
Hartree-Fock[g]	22.7		4.0
Hartree-Fock plus correlation[g]	14.0		3.1

[a]Reference 12.
[b]Reference 13.
[c]Reference 10.
[d]Reference 8.
[e]Reference 9.
[f]Reference 24.
[g]Reference 25.

we used the nonlinear core correction for lithium.[40] This correction was not needed when generating CPP-based pseudopotentials, which were not of density-functional origin. In the LDA, the LiF band gap was 8.7 eV, the F $2p$ bandwidth was 3.1 eV, and the centroid of the F $2s$ band was 19.0 eV below the VBM. These LDA results for band energies fell within 3% of the results of three other LDA calculations done in the pseudopotential, plane-wave,[41] pseudopotential, mixed-basis,[42] and full-potential, linear muffin-tin orbital[43] methods. Also, we predicted the structural properties of LiF with an accuracy to be expected for LDA results.

The quasiparticle results yielded considerable improvement over LDA results regarding agreement with experiment for the band gap, the F $2p$ bandwidth, and the F $2s$ to F $2p$ splitting. The band gap was 14.4 eV, the bandwidth 3.6 eV, and the centroid of the F $2s$ band lay 21.7 eV below the VBM. These results corroborate the suggestion, by Himpsel *et al.*,[10] that the F $2p$ band is wider than predicted by density-functional theory. In Table I we summarize results for LiF that are discussed in this section. In Fig. 1 we plot quasiparticle F $2s$ and F $2p$ bands.

Regarding the *GW* approximation's giving a larger F $2p$ bandwidth than the LDA, similar results occur in other materials, such as C_{60},[44] LiCl,[45] and CaF_2. It is useful, when discussing many-body effects on the bandwidths in insulators, to describe the replacement of the LDA with the *GW* approximation in two parts. First, there is the replacement of the LDA with the Hartree-Fock approach which treats exchange exactly but neglects correlation altogether. Second, there is the inclusion of correlation effects at some level of approximation. The bandwidths given by the Hartree-Fock approach are similar to those given by the *GW* approximation, so they are also larger than the bandwidths given by the LDA. Correlation effects do not necessarily narrow a bandwidth from Hartree-Fock results. Indeed, within model Hamiltonians, we have found instances of correlation effects increasing bandwidths.

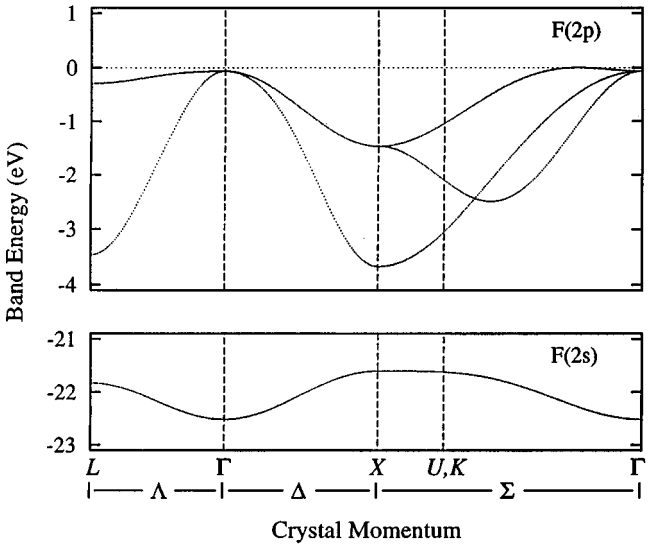

FIG. 1. LiF, F $2s$, and F $2p$ energy bands, plotted along the Λ, Δ, and Σ lines in the Brillouin zone. These bands are based on a Slater-Koster fit to quasiparticle results. (That the Slater-Koster VBM is on the Σ line rather than precisely at Γ is an artifact of the fit.)

Underestimation by the LDA of bandwidths in insulators appears to follow from its treatment of exchange. The LDA incorrectly allows a particle to ''see'' its own Hartree potential. (Note that the Hartree-Fock approach does not permit this.) Meanwhile, within a given band, lower-energy states tend to be more localized to atomic or molecular sites. Thus, for a filled band in an insulator, the errors arising from the LDA treatment of exchange will tend to be more positive near the bottom of the band, leading to underestimation of the bandwidth.

This notion does no resolve the related issues that occur in metals where the LDA gives occupied widths for partially filled bands that are too large.[46] Also, the widths of unoccupied bands in insulators are wider than obtained in the LDA, once many-body corrections are included. Northrup, Surh, Hybertsen, and Louie found a means of obtaining narrower bands in the *GW* approximation, but only if treating certain correlation effects in a somewhat inconsistent fashion. However, the results by Northrup, Surh, Hybertsen, and Louie are, to date, the most accurate, so these issues remain somewhat unresolved.

D. Slater-Koster description of electron initial states

The PAD's were computed by parametrizing the quasiparticle results for the F $2p$ bands using an orthogonal, tight-binding model, based on the approach of Slater and Koster.[17] We used a basis set of Li $2s$, Li $2p$, F $2s$, and F $2p$ atomic orbitals and coupled Li orbitals to those on the nearest F and Li and vice versa. We adjusted Slater-Koster parameters to maximize the agreement between the tight-binding and quasiparticle band energies. Using as a figure of merit the largest discrepancy in band-energy differences, the best results for

energies at Γ, X, and L gave a F $2p$ bandwidth of 3.4 eV. Meanwhile, the root-mean-square deviation of the tight-binding energies from their quasiparticle counterparts was 0.05 eV. However, since the widest band was the most prominent in PAD's, we chose to use Slater-Koster parameters that were uniformly scaled to give a 3.6-eV total bandwidth. Effects of this scaling on theoretical PAD's were minor, except near the bottom of the F $2p$ bands.

E. Nearly-free-electron description of final states

We include crystal-field effects on the electron final state within a nearly-free-electron picture. We use the crystal potential given by the LDA pseudopotential calculations, thereby including Bragg-diffraction effects arising from the low-order Fourier components of the crystal potential. These diffraction effects influence PAD's substantially, leading, among other things, to zone-selection effects (to be defined in Sec. VI A). The approach also neglects some other scattering effects of ion cores, especially for higher-energy photoelectrons and for partial waves with high angular momenta. Neglected effects may be treated more accurately using real-space, multiple-scattering theory.[47,48] However, these effects would introduce a relatively weak, smooth modulation of contrast in PAD's and this modulation would be similar for all electron initial states in the F $2p$ bands. (The F $2p$ bandwidth is only 4% of the lowest photon energy used in obtaining the PAD's we model.) The strongest contrast in PAD's arises from kinematical requirements of energy and momentum conservation, as well as matrix-element effects, and the F $2p$ PAD's change dramatically as the electron initial-state energy is varied throughout the F $2p$ band.

The nearly-free-electron Hamiltonian that was used in our calculations is defined as follows. Let us label a reciprocal-lattice vector with index $\mathbf{G}$ and its Fourier component of the crystal potential $V(\mathbf{G})$. We treat the $\mathbf{G}=0$ component separately, expressing it as an electrostatic energy $-eV_0$ plus a complex self-energy Σ. We abbreviate $-eV_0$ plus the real part of Σ by $U=-eV_0+\Sigma'$. So nearly-free-electron (NFE) dynamics are governed by this Hamiltonian

$$\hat{\mathbf{H}}_{\mathrm{NFE}}=-\frac{\hbar^2}{2m}\nabla^2-eV_0+\Sigma+\sum_{\mathbf{G}\neq\mathbf{0}}V(\mathbf{G})e^{i\mathbf{G}\cdot\mathbf{r}}-e\phi_{\mathrm{vac}}.$$

Here, ϕ_{vac} is the vacuum potential. We neglect the nonlocal parts of pseudopotentials in this Hamiltonian. Presumably, this is not a substantial approximation, when compared to the others made.

IV. MODEL FOR PHOTOELECTRON ANGULAR DISTRIBUTIONS

A. Kinematical considerations

In angle-resolved, photoelectron spectroscopic studies of materials, one measures the photocurrent for electrons with a given energy—call it E_{final}—with the two components of wave vector parallel to the surface specified. Call these components $p_{\parallel}^{(1)}$ and $p_{\parallel}^{(2)}$. In the vacuum, the third wave-vector component $p_{\perp}$ is known from the relation

$$E_{\mathrm{final}}=\frac{\hbar^2}{2m}[(p_{\parallel}^{(1)})^2+(p_{\parallel}^{(2)})^2+p_{\perp}^2]-e\phi_{\mathrm{vac}}.$$

Let us denote wave vector in the solid by $\mathbf{q}$. Varying the vacuum kinetic energy and exit direction of photoelectrons detected, one selects the energy, $q_{\parallel}^{(1)}$ and $q_{\parallel}^{(2)}$ of states probed. For periodic crystals, these two wave-vector components are given by $q_{\parallel}^{(1)}=p_{\parallel}^{(1)}$ and $q_{\parallel}^{(2)}=p_{\parallel}^{(2)}$, modulo surface umklapp effects. On the other hand, surface termination and lifetime effects prevent $q_{\perp}$ from being a good quantum number in the solid. However, the nearly parabolic dispersion for moderate-energy photoelectrons, say, those with vacuum kinetic energies exceeding 50 eV, restricts $q_{\perp}$ to a narrow range of values and thus renders the associated $\mathbf{p}$ values useful for probing the third momentum dimension. The typical value of $q_{\perp}$ may be selected by varying photon energy.

The present PAD's are computed, for several electron initial-state energies, with continuous sampling of $q_{\parallel}^{(1)}$ and $q_{\parallel}^{(2)}$. Band-dispersion effects are the chief mechanism behind contrast in the PAD's, and photoelectron diffraction effects are of secondary importance.

B. Treatment of surface effects

PAD's are influenced by the behavior of electron states near surfaces. For simplicity, we assume a spatially abrupt transition between vacuum and bulk environments. Complex surface termination can complicate PAD's,[49] but LiF(100) should have a nearly ideal termination. Since LiF is a wide-gap ionic insulator, the electron charge density should be bulklike even very close to the surface. Nonetheless, effects may arise from surface electronic states and even an ideal termination should perturb the crystal potential from its bulk value at finite proximity to the surface.

With the VBM approximately equal to 11 eV below the vacuum zero,[11] we neglect highly evanescent vacuum tails of electron initial states. Because valence-band F $2p$ holes are presumably long lived, we also neglect any imaginary parts of electron initial-state self-energies. So electron initial states can have a good $q_{\perp}$ within the solid, except that they form spatially undamped standing waves to accommodate crystal termination. An electron final-state wave function is a plane wave in the vacuum, but it is evanescent in the solid (via the imaginary part of its self-energy) and exhibits spatial modulation on the scale of the unit cell similar to that exhibited by wave functions for equal-energy conduction-band states in the bulk solid. The electron final-state wave function is continuously differentiable at the surface.

For PAD's, one seeks the vacuum amplitude of the electron final state, which determines the likelihood of a photoelectron's leaving a solid. However, a photoexcitation matrix element between electron initial and final states depends on the corresponding wave functions in the solid. It is straightforward to compute a photoexcitation matrix element in the bulk, where crystal momentum is a good quantum number and must be conserved. For the present electron final states, evanescence produces uncertainty in $q_{\perp}$ in the solid. The decay length for the electron final-state wave function in the direction normal to the surface is the normal band velocity divided by the imaginary part of the self-energy. A single evanescent electron final state can couple to many electron initial states having a spectrum of values of $q_{\perp}$. Photoexcitation matrix elements for couplings involving different values of the initial state $q_{\perp}$ may be approximately related to

matrix elements for the corresponding bulk states. Summation over values of the electron initial state $q_\perp$ is essentially independent of whether one sums over the above-mentioned standing waves or one sums over states with different values of $q_\perp$ without paying special attention to the presence of a surface. (Note that this sum over electron initial state $q_\perp$ is veritably a sum over system final states.)

C. Other experimental considerations

PAD's were affected by the transmission function of the detector. Instrumental and other uncertainties introduced an estimated 0.1 eV (full width at half maximum) Gaussian broadening of photoelectron energy distributions, which should be used to convolute the ideal transmission function, which was set to accept electrons within a 0.4-eV energy window. However, comparison of theoretical and experimental PAD's was improved dramatically when a much higher level of experimental broadening was invoked. As results depended weakly on the precise profile of the assumed energy-pass function, we used a detecting efficiency $Z(E_{\text{final}}-E_0)$ for an electron with energy E_{final} and the energy window centered at E_0, with $Z(x)=\exp[-x^2/(2\sigma^2)]$, and the optimal σ was 0.725 eV. Introducing such a level of uncertainty in the simulations is actually quite reasonable since defects or impurities in the LiF crystal could induce local, Fermi-level pinning, thus changing the local energy reference and accompanying resolution. So with the Z function included in our modeling of PAD's, the detector sampled electron final states in a so-defined range of energies and with so-defined quantum efficiencies.

Because of finite energy and angular resolutions and the uncertainty (broadening) in $q_\perp$, each pixel in an experimental PAD's image represented a collection of electron initial states in a region of the Brillouin zone. Energy-resolution effects were accounted for by incorporating the above Z function in the results; uncertainty in $q_\perp$ necessitated integration over $q_\perp$. (Note that energy-conservation requirements served to control the range of $q_\perp$ which is weighted heavily in a given electron final state.) Finite angular resolution was simulated by convolution of computed PAD's in the $q_\parallel$ directions. This convolution obfuscated most complications that follow logically from this simple fact: for most emission directions, when E_{final}, $p_\parallel^{(1)}$, $p_\parallel^{(2)}$, or $p_\perp$ changes, the other three quantities change with it.

Simulated PAD's computed as photocurrent per $(p_\parallel^{(1)},p_\parallel^{(2)})$ element were multiplied by $p_\perp$ for comparison with what was measured: photocurrent per solid angle. The experimental PAD's we consider have already been normalized to PAD's for secondary electrons having similar E_{final}. Some photoelectron-diffraction effects, angular distortion by the detector, and photon-flux inhomogeneities were partially compensated by this procedure. Subtracting a flat, experimental "base line" in the renormalized PAD's could, in principle, remove the secondary-electron signal; the height of this base line would depend on E. Final-state Bragg-diffraction effects on PAD's should not be canceled by this normalization, because such diffraction effects depend on a certain coherence in one's wave function, whereas such coherence is presumably absent in secondary-electron wave functions.

In matching the parameters of our model to the experiment, we incorporated damping effects based on an elastic mean free path of 5 Å estimated from the "universal curve."[50] This would mean a resolution in $q_\perp$ of about 0.2 Å^{-1}. On the other hand, the PAD's modeled sampled states clustered near the (300) or (400) Bragg planes, which were separated by about 1.56 Å^{-1}. The effective $q_\perp$ resolution was further reduced by finite energy resolution. At normal emission, we knew empirically that the central value of $q_\perp$ for states probed was, for electron initial states at the top or bottom of the F $2p$ band, at either a zone center or zone boundary, respectively: the photon energy had been chosen to achieve this. Correspondingly, our values of U in the nearly-free-electron Hamiltonian (one value for each photon energy) was chosen to make the initial-state energy at the respective zone center or boundary, plus $h\nu$, equal to the nearly-free-electron energy for such a value of crystal momentum.

D. Constituents of the present model

With the above considerations, we motivate the formulas used to compute PAD's. We first consider the problem of an excited electron leaving a semi-infinite, uniform solid. Effects of the crystal potential and complex electron self-energy are addressed. This problem is first solved in real space. Next, Fourier analysis of the result yields the admixture, in an evanescent, electron, final-state wave function, of a free-electron-like state with some **q** in the solid. This admixture is related to the electron propagator for such an energy-momentum combination in the bulk material.

We next provide formulas for photoexcitation matrix elements, appropriate in bulk situations, for excitations from valence bands to conduction bands lying in the same energy range as the photoelectrons we study. In the nearly-free-electron approach, a conduction-band wave function is approximated by a limited summation over its Fourier components: it is described as a few plane waves. Correspondingly, in the tight-binding approach, an electron, initial-wave function is described as the Bloch sums of a few atomic orbitals. We discuss how "$\mathbf{p}\cdot\mathbf{A}$" matrix elements between electron initial states and plane waves are computed; linear combinations of these objects form photoexcitation matrix elements.

We then consider extensions, related to the complications present in a real solid, to the description of an excited electron leaving a semi-infinite crystal. Many salient features of the uniform-solid illustration are retained. PAD's may still be modeled with the aid of the bulk electron propagator. However, the electron propagator is complicated by the variation (on the scale of the crystal unit cell) of the electron final-state wave function. Changes in the bulk electron propagator should reasonably account for most of the changes in PAD's. Indeed, the propagator for wave vector **q** neatly expresses the coherent superposition of the contributions by various channels—really, the equivalents of nearly-free-electron bands in a bulk system—to the photoelectron vacuum amplitude that results from photoexcitation of an electron initially in the valence band and having wave vector **q**. Finally, by combining single-plane-wave photoexcitation matrix elements with the electron propagator and including effects of integration over $q_\perp$ and the detector's transmission function, we arrive at the formula used for simulating PAD's.

E. Excited electron leaving a semi-infinite, uniform solid

Consider a semi-infinite uniform solid with an electrostatic potential V_0 relative to vacuum potential. In the solid, an electron experiences a self-energy because of screening and other many-body effects, adequately described by a homogeneous, local, complex effective potential $\Sigma=\Sigma'+i\Sigma''$. Abbreviate $U=-eV_0+\Sigma'$. Coordinates are labeled so that the surface lies in the yz plane at $x=0$, with the solid on the negative-x side. Components of the electron's wave vector parallel to the surface, $q_\parallel^{(1)}$ and $q_\parallel^{(2)}$, may be taken as good quantum numbers and the dynamics of the electron in the x direction may be solved separately. In solving these dynamics, consider the abbreviation

$$E_{\text{final}}+e\phi_{\text{vac}}=\epsilon+\frac{\hbar^2}{2m}[(q_\parallel^{(1)})^2+(q_\parallel^{(2)})^2].$$

Mathematically, it would be possible to have $\epsilon<0$. We have only dealt with combinations of E_{final}, $q_\parallel^{(1)}$, and $q_\parallel^{(2)}$, so that we had $\epsilon>0$. We limit our discussion to such circumstances.[51]

For an excited electron leaving the solid, the electron propagator may be written as

$$T^0(\mathbf{r},\mathbf{r}';E)=e^{iq_\parallel^{(1)}(y-y')}e^{iq_\parallel^{(2)}(z-z')}S^0(x,x';\epsilon).$$

It obeys the Dyson equation, which, for S^0, may be written as

$$\left[\epsilon+\frac{\hbar^2}{2m}\frac{\partial^2}{\partial x^2}-(U+i\Sigma'')\Theta(-x)\right]S^0(x,x';\epsilon)=\delta(x-x')$$

and

$$\left[\epsilon+\frac{\hbar^2}{2m}\frac{\partial^2}{\partial x'^2}-(U+i\Sigma'')\Theta(-x')\right]S^0(x,x';\epsilon)=\delta(x-x').$$

Here $\Theta(x)$ is the Heaviside function; which is equal to unity for $x>0$ and zero otherwise. The zero superscripts remind us that we are working presently with a uniform solid.

We wish to evaluate S^0. Causality implies a wave initially radiating from x' in both directions (toward and away from the surface). In the solid, it is damped. Upon reaching the surface, the wave is partially reflected, whereas the part transmitted into the vacuum propagates indefinitely without further damping. For $x'<0$, we find

$$\frac{\hbar^2}{m}S^0(x,x';\epsilon)=[Ae^{ik|x-x'|}e^{-\kappa|x-x'|}+Be^{ik|x|}e^{ik|x'|}e^{-\kappa|x|}e^{-\kappa|x'|}]\Theta(-x)+[Ce^{iK|x|}e^{(ik-\kappa)|x'|}]\Theta(x).$$

By satisfying the Dyson equation, including the "$x=x'$" and "$x=0$" boundary conditions, one finds

$$A=\left(\frac{1}{ik-\kappa}\right),$$

$$B=\left(\frac{i(k-K)-\kappa}{(ik-\kappa)(ik+iK-\kappa)}\right),$$

and

$$C=\left(\frac{2}{ik+iK-\kappa}\right).$$

We have defined

$$K\equiv p_\perp=\left[\frac{2m\epsilon}{\hbar^2}\right]^{1/2},$$

$$k^2-\kappa^2=\frac{2m}{\hbar^2}(\epsilon-U),$$

$$\frac{\hbar^2}{m}k\kappa=|\Sigma''|.$$

If we have $\epsilon>0$, then K, k, and κ may be taken as real, positive numbers. In that case, the above results show that, for $x'<0$ and $x>0$, we have

$$\frac{\hbar^2}{m}S^0(x,x';\epsilon)=e^{iKx}e^{(ik-\kappa)|x'|}\left(\frac{2}{ik+iK-\kappa}\right).$$

The Fourier transform of T_0 involves the transform of S^0. Consider the transform of $s(x,x')$ with respect to x and x', where E (and ϵ) are specified:

$$s(x,x')=\Theta(-x)\Theta(-x')S^0(x,x';\epsilon).$$

That is, we seek

$$\frac{\tilde{s}(q,q')}{[m/\hbar^2]}=\frac{1}{L}\int_{-L}^{0}dx\,e^{-iqx}\int_{-L}^{0}dx'\,e^{+zq'x'}\times[Ae^{ik|x-x'|}e^{-\kappa|x-x'|}+Be^{(ik-\kappa)|x|}e^{(ik-\kappa)|x'|}].$$

Here L is the thickness of our solid in the x direction and we take the $L\to\infty$ limit. For large L, we find

$$\frac{\tilde{s}(q,q')}{[m/\hbar^2]}=A\delta_{qq'}\left(\frac{1}{\kappa-ik-iq}+\frac{1}{\kappa-ik+iq}\right)+O(A/L)+\frac{B}{L}\left(\frac{1}{\kappa-ik-iq}\right)\left(\frac{1}{\kappa-ik+iq'}\right).$$

Let us combine the fractions in the first term. From the formulas for A, B, and C, one finds

$$\tilde{s}(q,q')=\frac{\delta_{qq'}}{(k^2-\kappa^2)/2+ik\kappa-q^2/2}+O(L^{-1}).$$

From further substitutions, we may deduce

$$\tilde{s}(q,q')=\frac{\delta_{qq'}}{E_{\text{final}}-\hbar^2/2m[(q_\parallel^{(1)})^2+(q_\parallel^{(2)})^2+q^2]+eV_0-\Sigma+e\phi_{\text{vac}}}+O(L^{-1}).$$

The first term in the above equation is the electron propagator in the bulk solid. Presumably, we may ignore terms $O(L^{-1})$ in the above equations. Such terms describe the following effects: (i) the electron's partial reflection at the surface (the term proportional to B) and (ii) the absence of

waves originating outside of the crystal (the term proportional to A). [Such waves would be present in the case of an infinite (versus finite) crystal.] If one ignores such terms, the last equation implies that the presence of a surface does not strongly influence electron states inside the solid. In particular, although such states must be standing waves, the electron propagator (which sums over such waves) is still ''diagonal'' in $q_\perp$.

The contribution to a PAD by an electron initial state with some $q_\perp$ is related to the Fourier transform of S^0 with respect to x' for the $x'<0<x$ situation. Namely, consider the formula

$$D(q_\perp)=\left(\frac{2}{ik+iK-\kappa}\right)\int_{-L}^{0}\frac{dx'}{L}\,e^{+iq_\perp x'}e^{(ik-\kappa)|x'|},$$

where we suppress trivial dependence of the result on x. For large L, we find

$$D(q_\perp)=\frac{2}{(ik+iK-\kappa)(\kappa-ik+iq_\perp)}\approx\frac{\hbar^2/2m}{E_{\rm final}-\hbar^2/2m[(q_\parallel^{(1)})^2+(q_\parallel^{(2)})^2+q_\perp^2]+eV_0-\Sigma+e\phi_{\rm vac}}.$$

Except for the factor $\hbar^2/2m$, this right-hand side is the bulk electron propagator for wave vector $\mathbf{q}$.

F. Bulk, interband, photoexcitation matrix elements

The photoexcitation matrix element between a bulk electron initial state $|\psi_i^{n\mathbf{q}}\rangle$ and an electron final state is linear combination of several matrix elements between the former state and individual plane waves. Such single-plane-wave matrix elements have been derived previously.[52,53] Here n is a band index and $\mathbf{q}$ is now a (crystal) wave vector. In the Slater-Koster description of the F $2p$ states, we have

$$\langle\mathbf{r}|\psi_i^{n\mathbf{q}}\rangle=\frac{1}{N^{1/2}}\sum_{\mathbf{R}}\,e^{i\mathbf{q}\cdot\mathbf{R}}\sum_{\mu}\,D_\mu^{n\mathbf{q}}\phi_\mu(\mathbf{r}-\mathbf{R}-\boldsymbol{\tau}_\mu).$$

We sum $\mathbf{R}$ over all N unit cells in a solid and consider the $N\to\infty$ limit. We sum μ over all ''atomic orbitals'' in each cell and the orbitals are described by the ϕ functions, with associated atoms located at the $\boldsymbol{\tau}_\mu$ basis vectors within each cell. Each $D_\mu^{n\mathbf{q}}$ is the expansion coefficient for orbital μ in state $|\psi_i^{n\mathbf{q}}\rangle$. Spin indices, irrelevant here, are suppressed. We separate radial and angular character of the ϕ's as

$$\phi_\mu(\mathbf{x})=f_\mu(|\mathbf{x}|)Y_\mu(\hat{\mathbf{x}}).$$

The Y_μ functions are angular harmonics.

Consider the maxtrix element

$$I_{\mathbf{K}}^{n\mathbf{q}}=\langle e^{i(\mathbf{G}+\mathbf{q})\cdot\mathbf{r}}|(\mathbf{p}\cdot\mathbf{A})|\psi_i^{n\mathbf{q}}\rangle.$$

We use the abbreviation $\mathbf{G}+\mathbf{k}=\mathbf{K}$. We may write this matrix element as

$$I_{\rm K}^{n\mathbf{q}}\propto(\mathbf{K}\cdot\boldsymbol{\epsilon})\sum_\mu\,D_\mu^{n\mathbf{q}}e^{-i\mathbf{K}\cdot\boldsymbol{\tau}_\mu}g_\mu(|\mathbf{K}|)Y_\mu(\hat{\mathbf{K}}).$$

(We suppress a proportionality constant.) The $D_\mu^{n\mathbf{q}}$ coefficients determine how atomic orbitals are weighted in the matrix element. For each orbital, g is a radial Fourier transform of f. For states originating from one kind of atomic orbitals, g might serve only to give an overall prefactor to PAD's. We found this to be true in this work, with g evaluated using Hartree-Fock atomic orbitals. However, when g varies sufficiently over a range of $|\mathbf{K}|$'s represented in the electron final state, then the presence of g might play a greater role in influencing PAD's.

The polarization factor $(\mathbf{K}\cdot\boldsymbol{\epsilon})$ is of interest, as is the factor $Y_\mu(\mathbf{K})$. Here $\boldsymbol{\epsilon}$ is the electric-field polarization vector. The former selects emission directions based on photon polarization, while the latter selects initial states based on an emission direction. For initial p states, the Y_μ factor indicates PAD's being dominated by states involving heavy weighting of the p orbital most parallel to $\mathbf{K}$. The phase factor of $\exp(-i\mathbf{K}\cdot\boldsymbol{\tau}_\mu)$ for each μ can produce interesting interference effects when a state is located on more than one atom in the unit cell. However, initial states in this work are essentially located on fluorine atoms only. Multiatom interference effects are substantial in the case of graphite[21] and in the case of CaF_2.

G. Excited electron leaving a semi-infinite, real solid

Consider first the role played by the vector $\mathbf{q}$ in the above problem of an excited electron leaving a uniform solid. An electron final state with vacuum wave vector $\mathbf{p}$ continues into a uniform solid with a momentum distribution determined by the evanescent solution that was derived above. We sampled this momentum distribution with the total momentum of the electron in the uniform solid $\hbar\mathbf{q}$. Furthermore, evanescence prevented $q_\perp$ from being a good quantum number. Note that the total *vacuum* wave vector of a detected photoelectron $\mathbf{p}$ was not restricted to the first Brillouin zone, nor was the value of $\mathbf{q}$.

Consider next one value in the continuum of values of $\mathbf{q}$ represented by the electron final state. Let us continue to consider $\mathbf{q}$ in an extended-zone picture. Heuristically, because of the crystal potential in a real solid, an electron final state may, in addition to amplitude for each value of $\mathbf{q}$ appropriate in the uniform-solid case, also have a nonzero amplitude for a wave vector $\mathbf{G}+\mathbf{q}$. Besides the fundamental $\mathbf{G}=\mathbf{0}$ reciprocal-lattice vector, we will consider the next few lowest stars of $\mathbf{G}$'s. We do not consider further elaboration of an evanescent electron final state than this generalization of each value of $\mathbf{q}$. Furthermore, this generalization will be made as prescribed by the bulk electron propagator. In other words, to estimate the crystal-field effects on a photoexcitation matrix element involving an evanescent photoelectron final state, we assume the corresponding effects that would occur for the corresponding bulk, photoexcitation matrix elements. In turn, these effects are estimated in this work using a nearly-free-electron picture. (We remind the reader that an electron, final-state wave function is continuously differentiable at the crystal surface, so the photoelectron vacuum

amplitude is still closely related to the "free-electron" part of any more elaborate propagator.)

We then arrive at an expression describing the contribution to the photoelectron vacuum amplitude from the electron initial state $|\psi_i^{n\mathbf{q}}\rangle$. This involves bulk, single-plane-wave matrix elements and the electron propagator. However, we now use the nearly-free-electron version thereof. Except for a proportionality constant, the photoelectron vacuum amplitude is given as

$$D^{n\mathbf{q}}(E_{\text{final}}) = \sum_{\mathbf{G}'} S_{\mathbf{G},\mathbf{G}'}(\mathbf{q},E_{\text{final}})|_{\mathbf{G}=\mathbf{0}} I^{n\mathbf{q}}{}_{\mathbf{G}'+\mathbf{q}}.$$

Here $S_{\mathbf{G},\mathbf{G}'}(\mathbf{q},E_{\text{final}})$ is a matrix element of the bulk, nearly-free-electron propagator. It is given by

$$S_{\mathbf{G},\mathbf{G}'}(\mathbf{q},E_{\text{final}}) = \left\langle \exp[i(\mathbf{G}+\mathbf{q})\cdot\mathbf{r}] \left| \frac{1}{E_{\text{final}}-\hat{H}_{\text{NFE}}} \right| \exp[i(\mathbf{G}'+\mathbf{q})\cdot\mathbf{r}] \right\rangle.$$

H. Formula for PAD's

For conciseness, we now write the formula used to compute PAD's, save for inclusion of finite-angular-resolution effects. We write the formula for the case, that the detector's energy-acceptance window is centered at energy E_0, and the emission angle corresponds to states with wave-vector components $q_\parallel^{(1)}$ and $q_\parallel^{(2)}$. Photocurrent per $(q_\parallel^{(1)},q_\parallel^{(2)})$ element is given as

$$\Phi(q_\parallel^{(1)},q_\parallel^{(2)};E_0) \propto \sum_n \int dq_\perp Z(\epsilon^{n\mathbf{q}}+h\nu-E_0) \times |D^{n\mathbf{q}}(\epsilon^{n\mathbf{q}}+h\nu)|^2.$$

V. THEORETICAL PHOTOELECTRON ANGULAR DISTRIBUTIONS, WITH COMPARISON TO EXPERIMENT

In Ref. 10, the F $2p$ bandwidth was determined according to the following scenario. For a given datum in a PAD, let us refer to the central value of $q_\perp$ as "$Q_\perp$." The PAD's were collected for LiF(100) using photon energies 85.5 and 152 eV. At normal emission, consequently, $Q_\perp$ coincides with the (300) and (400) Bragg planes, respectively (cf. Fig. 2). (We indicate these planes in units of $2\pi/a$, where a is the lattice constant.) For large portions of the PAD's, in particular, close to normal emission, $Q_\perp$ would have remained close to one of these Bragg planes. Furthermore, the strongest features in the PAD's were to be found near normal emission. Near the (N00) Bragg planes, symmetry implied that the fluorine $2p_x$ orbitals did not couple strongly to the $2p_y$ or $2p_z$ orbitals, when Bloch sums of these three atomic orbitals were combined to form each state, $|\psi_i^{n\mathbf{q}}\rangle$. So one band could be distinguished from the other two bands near an (N00) Bragg plane and, in such regions of reciprocal space, we label this band the "$2p_x$" band. Meanwhile, this $2p_x$ band was preeminent in PAD's, a consequence of the Y factors in formulas

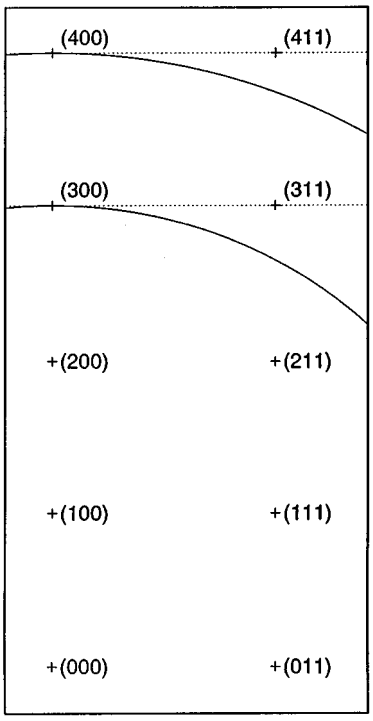

FIG. 2. Constant-wave-number contours (solid lines), drawn in reciprocal space, along with several wave vectors (written in units of $2\pi/a$, where a is the lattice constant). At normal emission for LiF(100), these contours are tangent to the (400) and (300) Bragg planes (dashed lines).

for photoexcitation matrix elements, and while the PAD's therefore illustrated constant-energy contours for this $2p_x$ band very plainly, this $2p_x$ band also spanned the entire F $2p$ bandwidth.

There are two types of X points in the (N00) Bragg planes. Zone boundaries, centers, and the two types of X points (X_1 and X_2) in such planes are illustrated in Fig. 3, in addition to energy contours for the $2p_x$ band. Because the reciprocal

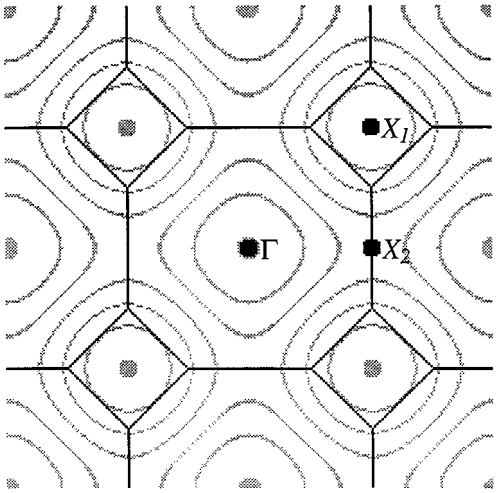

FIG. 3. Brillouin-zone boundaries (black) and zone and zone-face centers that are found in an (N00) Bragg plane. In addition, at intervals of 0.6 eV, from −3.6 to 0.0 eV (VBM), we indicate constant-energy contours for the "$2p_x$ band" (cf. the text), where each contour has a 0.06 eV width.

lattice for LiF is body-centered cubic, either an X_1 point or a zone center was sampled at normal emission in the PAD's described. In the present Slater-Koster approach, the $2p_x$ band energy in an $(N00)$ plane is approximated as

$$\epsilon^{n\mathbf{q}}(2p_x) \approx \epsilon_0 - 4\cos\left(\frac{q_y a}{2}\right)\cos\left(\frac{q_z a}{2}\right)|V_{pp}^{\pi}| + 2\cos\left(\frac{q_x a}{2}\right) \times\left[\cos\left(\frac{q_y a}{2}\right)+\cos\left(\frac{q_z a}{2}\right)\right](|V_{pp}^{\sigma}|-|V_{pp}^{\pi}|).$$

(The primary mechanism underlying the F $2p$ bandwidth is interatomic, F $2p$ to F $2p$ hybridization.) Here ϵ_0 is to be understood as an F $2p$ term energy and we otherwise use standard Slater-Koster formalism, except that we avoid all possible confusion regarding the effective signs of the tight-binding parameters. Meanwhile, consider the F $2p$ bands presented in Fig. 1. Dispersion of the $2p_x$ band in the (011)-type directions is the same as that of the band that, along the Σ line from Γ to $X(X_1)$, spans the entire F $2p$ bandwidth. Dispersion of the $2p_x$ band in the (010)-type directions is the same as that of the twofold degenerate, upper bands along the Δ line from Γ to X (X_2).

Of course, our model for PAD's also reflects many other physical effects discussed in Sec. IV. Quantitative changes in PAD's, associated with these physical effects, can be quite complicated. Some readily anticipated effects include the appearance of other bands off of normal emission, arising from changes in the Y factors, from departure of $Q_\perp$ from the Bragg planes, and from the imperfect knowledge of $q_\perp$. In addition, other matrix element effects including those relating to the multiple-plane-wave character of final states should play a role. These last considerations lead to zone-selection effects, which are analyzed in Sec. VI.

In the remainder of this section we present theoretical and experimental PAD's and examine the level of agreement between them. The experimental data are those reported in Ref. 10. These images have been normalized as discussed in Sec. IV and symmetrized according to the C_{4v} symmetry[54] of the LiF(100) surface. The incident photons were predominantly s polarized and incident at 45°. The symmetrizations of the data rendered the azimuthal angle of photon incidence irrelevant. We included all effects regarding photon incidence and symmetrization when computing PAD's.

Gray-scale images provide an efficacious rendering of modulation in the electron flux per energy solid angle, which is how the present PAD's are presented. However, they are presented as functions of $q_\parallel^{(1)}$ and $q_\parallel^{(2)}$. The gray-scale rendering of PAD's has also been widely used in (core-level) photoelectron diffraction and holography studies of materials. PAD's were computed on a coarse mesh in $q_\parallel^{(1)}$ and $q_\parallel^{(2)}$ and interpolated onto a finer mesh. Empirically, we found this had a negligible effect on PAD's. Finite angular resolution was simulated by convolution of theoretical PAD's, with respect to $q_\parallel^{(1)}$ and $q_\parallel^{(2)}$, using a Gaussian with a full width at half maximum of 0.3 Å^{-1}. This corresponds to an angular resolution of 2° or 3°, a poorer resolution than that which is intrinsic to the apparatus. This particular resolution was chosen to maximize agreement between the theoretical and experimental PAD's. Such an apparent degradation of experimental, angular resolution might arise partly from charging in the sample.

In Fig. 4 we consider the PAD for $h\nu = 152$ eV, and for $E = -2.3$ eV. Theoretical results are shown for the inclusion of 1 **G**-vector, 15 **G**-vectors, and 65 **G**-vectors in the nearly-free-electron, final-state wave functions. For the cases of 1 **G**-vector and 65 **G**-vectors we also show PAD's computed when $q_\perp$ samples only $Q_\perp$. In all other theoretical PAD's, $q_\perp$ was integrated, in 99 steps, from $Q_\perp - 2\pi/a$ to $Q_\perp + 2\pi/a$. (Based on convergence tests, both this range and detail of sampling proved adequate.) We also show the experimental PAD and a "split-image" PAD, which features the best (65 **G**-vectors plus $q_\perp$ integration) theoretical PAD and its experimental counterpart juxtaposed, for comparison, with half of each PAD shown on opposite sides of a (010)-mirror plane. In split images of this type, the theoretical half is shown below the experimental half. Perfect agreement between the two would produce PAD's with top-bottom mirror symmetry; imperfect agreement causes this symmetry to be broken.

A given PAD includes a set of N pixels, each pixel denoted by index p. Each pixel corresponds to a $(q_\parallel^{(1)}, q_\parallel^{(2)})$ element. The range of phase space sampled in a PAD is determined by the acceptance angle of the electron analyzer, sample orientation, and avoidance of spurious signals which arise near the edge of the field of view (i.e., limitation of the angles actually surveyed). For each pixel, we denote the experimental or theoretical photocurrent per solid angle as E_p or T_p, respectively. When comparing PAD's, one should consider overall normalization and base-line subtraction. Since these effects might vary from PAD to PAD, we allow for a separate adjustment in each PAD of the normalization and base-line height. The adjustment was based on minimizing

$$\sum_p |T_p - A - BE_p|^2$$

with respect to fitting parameters A and B. Agreement between the experimental and theoretical data was estimated using a standard, linear regression correlation coefficient,[55]

$$\rho = \frac{\Sigma_p E_p T_p/N - (\Sigma_p E_p/N)(\Sigma_p T_p/N)}{\{[\Sigma_p E_p^2/N - (\Sigma_p E_p/N)^2][\Sigma_p T_p^2/N - (\Sigma_p T_p/N)^2]\}^{1/2}}.$$

This ρ is independent of (positively signed) normalizations and base-line subtractions and is confined to the range -1 to 1. (This fact is related to the Cauchy-Schmidt inequality.)

Each theoretical and experimental PAD had its counterpart. A split-image PAD involved a theoretical PAD, described by $\{T_p\}$ and a scaled version of the corresponding, experimental PAD, described by $\{E'_p\} = \{A + BE_p\}$. For every split image, the gray scale was adjusted so that the image spanned the full dynamic range of that scale, but neither the experimental nor the theoretical image had substantial portions saturated at either end of that scale. (The same adjustment was made in both halves of each split image, i.e., for T_p and E'_p.) To produce the all-theory or all-experiment PAD's shown in Fig. 4, we began with split images, and their associated gray scales, and reflected these to display only the experimental or theoretical parts.

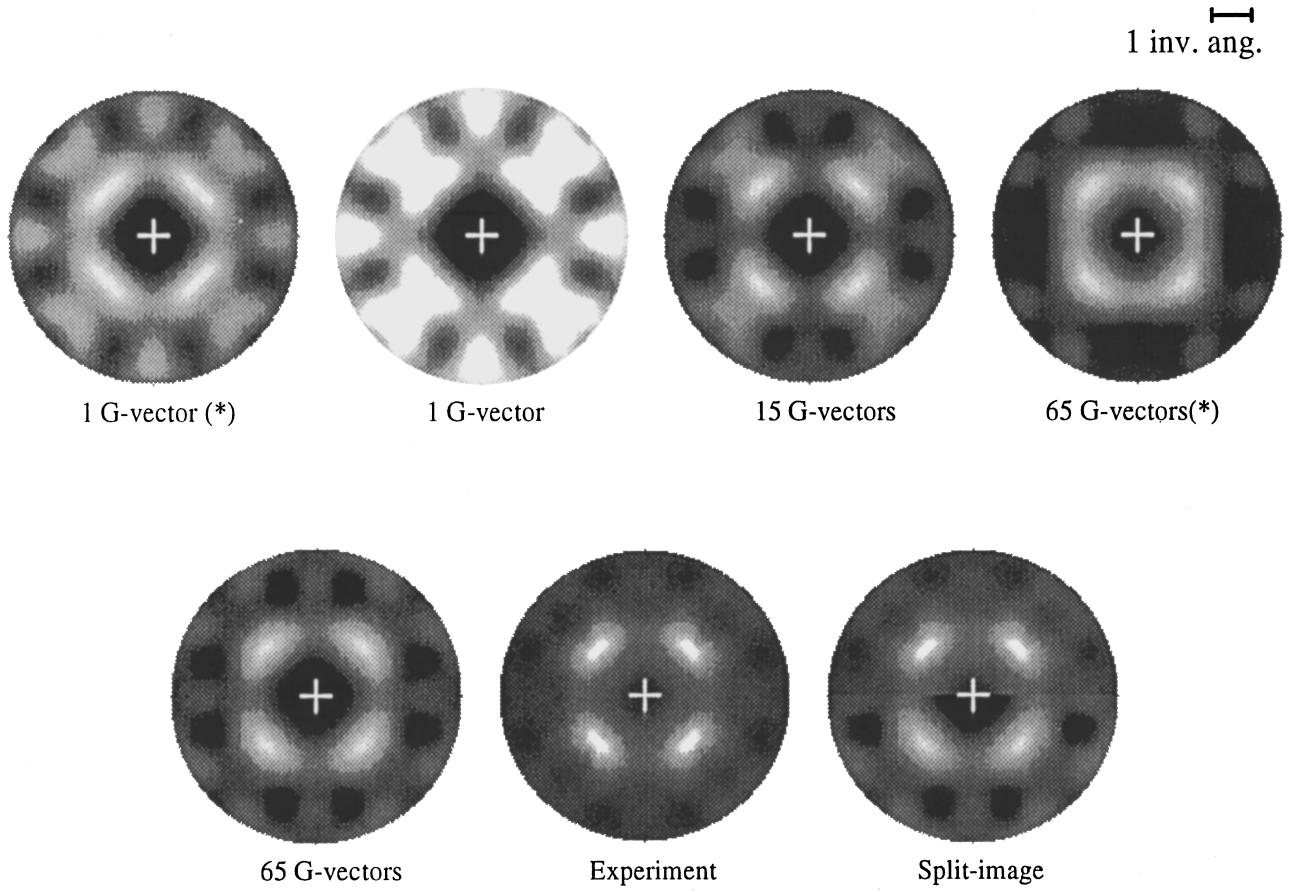

FIG. 4. For $h\nu = 152$ eV, $E = -2.3$ eV, theoretical PAD's using various numbers of **G** vectors in the nearly-free-electron description of photoelectron final states. Also shown are an experimental PAD and a split-image having theory (bottom) and experiment (top) juxtaposed. An asterisk indicates that no $q_\perp$ has been performed in computing a given PAD. Note the wave-vector scale. Cartesian coordinates are as shown in Fig. 3. A cross denotes the normal-emission direction. Higher-flux areas are shown more brightly.

In Fig. 5, split images are presented for every PAD given in Ref. 10. In Table II, we present results for the correlation coefficients between the theoretical and experimental PAD's. As a control, correlation coefficients are given between all experimental and all theoretical PAD's for each photon energy and not only between each experimental PAD and its unique theoretical counterpart. Evidently, one can use the correlation coefficients tabulated in Table II to associate the experimental PAD's with the correct theoretical counterparts. (This might not be true when two distinct PAD's are quite similar, such as when the two PAD's are for similar energies.) In Table III we present correlation coefficients for each experimental PAD and its theoretical counterpart and for PAD's computed according to the various approaches represented in Fig. 4.

VI. DISCUSSION

In Fig. 5, note the remarkable level of similarity between the experimental and theoretical images of PAD's, not only in the strongest features, but also in the weaker features. On a more quantitative note, consider the results in Table III. Evidently, computed PAD's are substantially influenced by both integration over $q_\perp$ and attention to Bragg-diffraction effects on electron final states. Whereas inclusion of Bragg-diffraction effects is clearly vital for achieving the highest level of accuracy, other diffraction effects that we neglect in our approach may also be significant. This is difficult to ascertain, however, partly because of our crude treatment of mean-free-path effects. Note that $q_\perp$-integration affects computed PAD's substantially, suggesting that a better treatment of mean-free-path effects could improve results. From the last two columns in Table III, one might surmise that mean-free-path effects are somehow being overestimated by the present treatment. Issues are also complicated by the present treatment of surface effects. However, aside from a more complete treatment of photoelectron diffraction effects, accomplishing the refinements to which we allude, in a fashion that is not *ad hoc*, would be beyond the scope of this work.

A. Low-order Bragg diffraction and zone-selection effects

The PAD's displayed in Figs. 4 and 5 represent contributions from states on both sides of the $(0,\pm1,0)$ and $(0,0,\pm1)$ Bragg planes. These planes correspond to $q_\parallel^{(i)} = \pm 2\pi/a \approx 1.56$ Å^{-1}, where i now indicates the y or z direction. In principle, portions of PAD's near these planes could exhibit mirror symmetry with respect to reflection

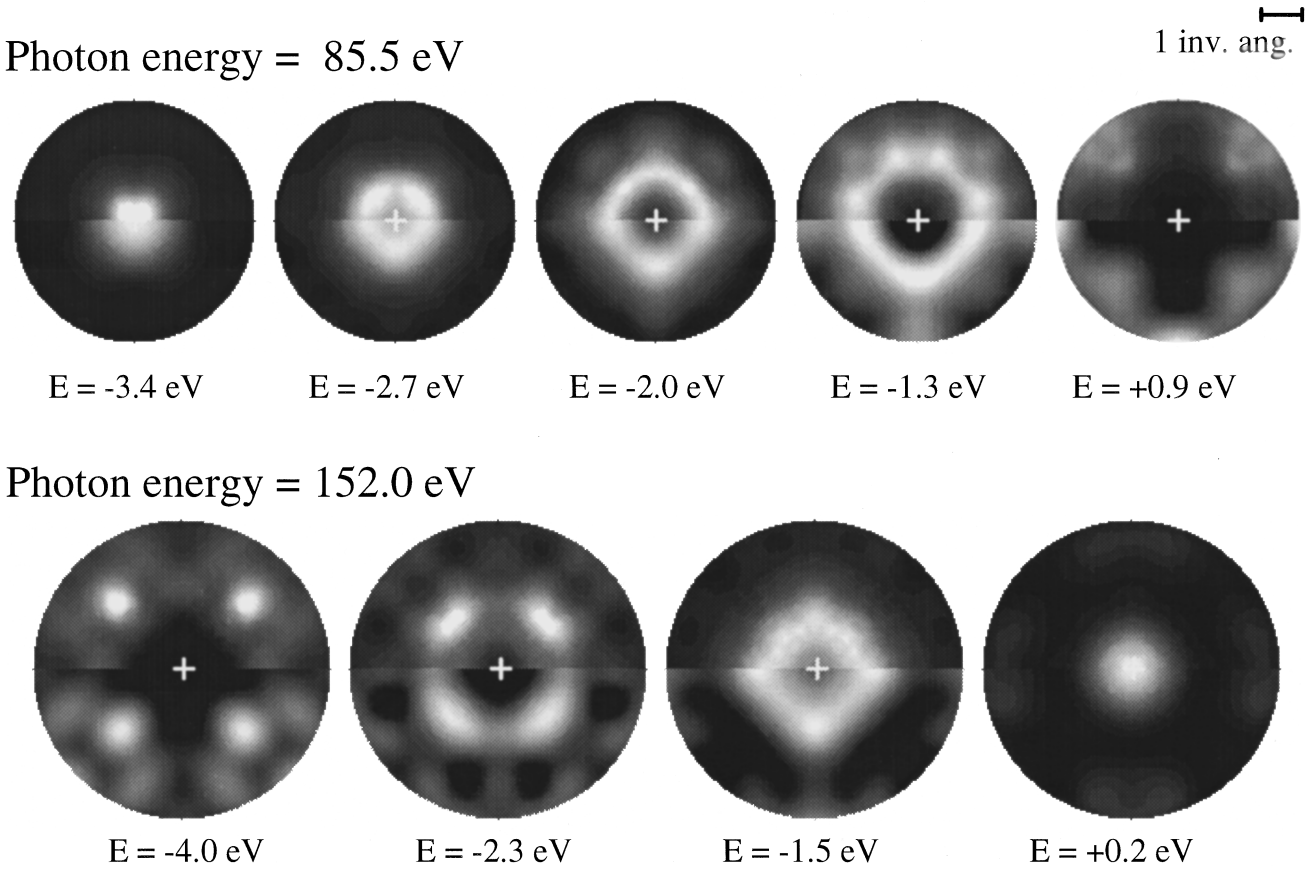

FIG. 5. For two photon energies and various initial states energies, split images of theoretical (bottom half) and experimental (top half) PAD's. Computational details are provided in the text. Note the wave-vector scale. Cartesian coordinates are as shown in Fig. 3. A cross denotes the normal-emission direction. Higher-flux areas are shown more brightly.

TABLE II. Correlation coefficients for comparison of theoretical and experimental PAD's. The theoretical and experimental PAD's are respectively indicated by initial-state energies E_{theor} and E_{expt}, given in eV relative to the VBM. Results are presented for two photon energies. Correlation coefficients for pairs of corresponding PAD's are underscored.

	E_{theor}				
E_{expt}	−3.4	−2.7	−2.0	−1.3	+0.9
	$h\nu = 85.5$ eV				
−3.4	0.96	0.79	0.36	−0.33	−0.42
−2.7	0.90	0.98	0.77	0.06	−0.59
−2.0	0.36	0.66	0.96	0.75	−0.71
−1.3	−0.28	−0.05	0.44	0.82	−0.46
+0.9	−0.52	−0.63	−0.72	−0.49	0.78
	$h\nu = 152$ eV				
	−4.0	−2.3		−1.5	−0.2
−4.0	0.85	0.29		−0.48	−0.50
−2.3	0.06	0.85		0.57	−0.11
−1.5	−0.58	0.20		0.91	0.54
+0.2	−0.52	−0.47		0.32	0.99

TABLE III. Correlation coefficients for comparison of experimental and theoretical PAD's, where theoretical PAD's correspond to including N_G reciprocal-lattice vectors in the nearly-free-electron model used for electron final states, and an asterisk denotes that no integration over $q_\perp$ has been performed. PAD's are identified by the photon energy and electron initial-state energy E, given relative to the VBM. The rightmost column corresponds to results presented in Table II and Fig. 5.

	N_G				
E (eV)	1*	1	15	65*	65
	$h\nu = 85.5$ eV				
−3.4	0.94	0.95	0.96	0.96	0.96
−2.7	0.97	0.97	0.98	0.99	0.98
−2.0	0.96	0.95	0.96	0.93	0.96
−1.3	0.91	0.84	0.84	0.74	0.82
+0.9	0.75	0.85	0.82	0.76	0.78
	1*	1	15	65*	65
	$h\nu = 152$ eV				
−4.0	0.74	0.50	0.86	0.84	0.85
−2.3	0.61	0.13	0.71	0.93	0.85
−1.5	0.85	0.65	0.85	0.94	0.91
+0.2	0.80	0.93	0.98	1.00	0.99

through the planes. However, this is found not to be the case. Instead, photoelectron flux is generally much more pronounced inside a $(4\pi/a)\times(4\pi/a)$ square centered around the normal emission direction and on the corresponding sides of those four Bragg planes. This breaking of symmetry often occurs along planes that coincide with zone boundaries. This effect is a result of photoelectron diffraction by low-order Fourier components of the crystal potential, and this zone-selection effect is already reproduced if our nearly-free-electron approximation is used when computing PAD's.

The zone-selection effect being discussed may largely be explained in a two-plane-wave model. Suppose that **q** is near *one* of the four Bragg planes, e.g., the (010) plane. In the wave functions of the conduction-band states, which are represented in the electron final state, two plane waves would be most heavily weighted in the nearly-free-electron approximation. One plane wave has wave vector **q**, which is close to the Bragg plane in reciprocal space, and the other plane wave has wave vector $\mathbf{G}+\mathbf{q}$, where **G** is the reciprocal-lattice vector $(0,-4\pi/a,0)$. Now in the photoemission process we are interested in the nearly-free-electron bands that most closely follow the free-electron dispersion relation (modulo a trivial energy shift). Let us choose our coordinates so that a fluorine atom is at the origin of our unit cell. Then for this **G**, $V(\mathbf{G})$ is both real and negative. Solution of the nearly-free-electron Hamiltonian in the two-plane-wave model amounts to the solution of a quantum-mechanical two-level system. In the nearly-free-electron states that are energetically closest to the free-electron dispersion curve, one find that on the same side of the (010) plane as the origin, Fourier components for wave vectors **q** and $\mathbf{G}+\mathbf{q}$ will have like signs and that on the other side of the (010) plane, these Fourier components will have the opposite signs.

The above admixture of the plane waves having wave vectors **q** and $\mathbf{G}+\mathbf{q}$ determines the weightings of the single-plane-wave matrix elements discussed earlier. According to these weightings and the relative signs of these single-plane-wave matrix elements, contributions to $D^{n\mathbf{q}}(E_{\text{final}})$ arising from various single-plane-wave matrix elements may interfere constructively or destructively. In an $(N00)$ plane, where N is greater than zero, and near the (010) plane, matrix elements between a fluorine $2p_x$ orbital and the two plane waves are nearly the same. Therefore, contributions to PAD's from states dominated by the $2p_x$ orbitals should be stronger on the same side of the (010) plane as the origin than on the other side. This is seen in the PAD's. Analogous matrix elements involving the $2p_y$ orbitals have one sign for the plane wave described by wave vector **q** and an opposite sign for the other plane wave. Therefore, contributions to PAD's from states dominated by the $2p_y$ orbitals should be weaker on the same side of the (010) plane as the origin than on the other side. Since the contributions from $2p_y$ and $2p_z$ orbitals are weak in the PAD's, the zone-selection effect for these contributions is barely discernible in the images.

VII. CONCLUSION

We have presented quasiparticle results for the band structure of LiF and simulated photoelectron angular distributions for the F $2p$ valence bands. The band gap, F $2p$ bandwidth, and F $2s$ to F $2p$ separation (defined as the energy difference between the F $2s$ centroid and valence-band maximum) were found to be 14.4, 3.6, and 21.7 eV, to be compared with the measured 14.2, 3.5, and 24.9 eV, respectively. Photoelectron angular distributions were computed using the quasiparticle results for the F $2p$ states. In this endeavor, photoelectron final states were modeled to include their evanescence in the solid plus their modulations on the scale of the unit cell. Effects of such modulations on photoexcitation matrix elements were extrapolated from the analogous effects that would occur in corresponding photoabsorption processes in bulk LiF. These latter effects were estimated for the bulk using the multiple-plane-wave character of isoenergy conduction-band states as found within a nearly-free-electron model.

Comparisons between experimental and theoretical photoelectron angular distributions were made by analyzing correlations in measured and predicted photocurrent per unit solid angle as a function of emission direction. On a range from -1 to 1, correlation coefficients varied between 0.78 and 0.99 in the final results for the nine PAD's that we examined. We suggest possible areas for improvement of the present model used to compute PAD's. In particular, we suggest that one could employ a more complete description of photoelectron diffraction, perhaps based on real-space multiple-scattering theory.

The results indicate the high level of detail, regarding a material's band structure, which may be inferred from photoelectron angular distributions. This is a positive outcome, considering current advances in synchrotron-radiation sources and electron-analyzer technology. In future work, detailed modeling of photoelectron angular distributions for valence bands could be an invaluable tool that closely accompanies experiments. In our attempts to probe the electronic structure of new materials, this may prove especially important in the study of novel and complex systems, including surfaces and heterojunctions.

Note added in proof. After submission of this manuscript, subsequent tests indicated that omission of nonlocal parts of pseudopotentials would have minimal effect on the results of this work. However, studies of other systems and/or based on different choices of local pseudopotential channels may exhibit a greater role for such nonlocal parts in final-state multiple-scattering processes.

ACKNOWLEDGMENTS

This work was conducted, in part, under the auspices of the U. S. Department of Energy, Office of Basic Energy Sciences, Division of Materials Science, by the Lawrence Livermore National Laboratory under Contract No. W-7405-ENG-48. We have benefited from fruitful discussions with C. S. Fadley, D. A. Shirley, J. N. Glosli, and L. H. Yang. In particular, we wish to thank M. P. Surh and L. H. Yang for providing local-density approximation band-structure results for LiF for comparison with, and verification of, the results presented here.

[1] For instance, see A. W. Moore, in *Chemistry and Physics of Carbon*, edited by P. L. Walker and P. A. Thrower (Dekker, New York, 1973), Vol. 17, p. 69.
[2] See, for example, K. J. Teegraden, Phys. Rev. **155**, 896 (1967).
[3] H. Vora, J. H. Jones, and T. G. Stoebe, J. Appl. Phys. **46**, 71 (1975); F. N. Cocks and I. T. A. Pollock, *ibid*. **43**, 3878 (1972).
[4] D. A. Lapiano-Smith, E. A. Eklund, F. J. Himpsel, and L. J. Terminello, Appl. Phys. Lett. **59**, 2174 (1991).
[5] J. C. Barton, C. J. Hatton, and J. E. McMillan, J. Phys. G **17**, 1885 (1991).
[6] P. I. Antonov, V. M. Krymov, and E. Hartmann, J. Cryst. Growth **104**, 142 (1990).
[7] A. Milgram and M. Parker Givens, Phys. Rev. **125**, 1506 (1962).
[8] M. Piacentini, D. W. Lynch, and C. G. Olson, Phys. Rev. B **13**, 5330 (1976).
[9] M. Piacentini, Solid State Commun. **17**, 697 (1975).
[10] F. J. Himpsel, L. J. Terminello, D. A. Lapiano-Smith, E. A. Eklund, and J. J. Barton, Phys. Rev. Lett. **68**, 3611 (1992).
[11] A. single-energy photoelectron angular distribution for F 2*s* state is presented in Ref. 4.
[12] There is an estimate of 14.5 eV in Ref. 9, a gap of 14.2 ± 0.2 eV was found in Ref. 8, and a gap of 14.1 ± 0.1 eV was determined from the onset of photoemission from single-crystal LiF(100) in F. J. Himpsel, Ph.D. thesis, University of Munich, 1976.
[13] S. P. Kowalczyk, F. R. McFeely, L. Ley, R. A. Pollak, and D. A. Shirley, Phys. Rev. B **9**, 3573 (1974).
[14] M. S. Hybertsen and S. G. Louie, Phys. Rev. Lett. **55**, 1418 (1985); Phys. Rev. B **34**, 5390 (1986).
[15] D. E. Eastman, J. J. Donelon, N. C. Hien, and F. J. Himpsel, Nucl. Instrum. Methods **172**, 327 (1980).
[16] R. L. Kurtz, S. W. Robey, L. T. Hudson, R. V. Smilgys, and R. L. Stockbauer, Nucl. Instrum. Methods Phys. Res. Sect. A **319**, 257 (1992); S. D. Kevan, Surf. Sci. **307–309**, 832 (1994); P. Aebi, J. Osterwalder, R. Fasel, D. Naumovic, and L. Schlabach, *ibid*. **307–309**, 917 (1994).
[17] J. C. Slater and G. F. Koster, Phys. Rev. **94**, 1498 (1954).
[18] W. E. Spicer, Phys. Rev. **112**, 114 (1958).
[19] G. D. Mahan, Phys. Rev. B **2**, 4334 (1970).
[20] P. J. Feibelman and D. E. Eastman, Phys. Rev. B **10**, 4932 (1974), and references therein.
[21] E. L. Shirley, L. J. Terminello, A. Santoni, and F. J. Himpsel, Phys. Rev. B **51**, 13 614 (1995).
[22] L. Hedin and S. Lundqvist, in *Solid State Physics*, edited by H. Ehrenreich, F. Seitz, and D. Turnbull (Academic, New York, 1969), Vol. 23, p. 1.
[23] P. Hohenberg and W. Kohn, Phys. Rev. **136**, 864 (1964); W. Kohn and L. J. Sham, *ibid*. **140**, 1133 (1965).
[24] A. Zunger and A. J. Freeman, Phys. Rev. B **16**, 2901 (1977).
[25] A. B. Kunz, Phys. Rev. B **26**, 2056 (1982).
[26] R. W. Godby, M. Schlüter, and L. J. Sham, Phys. Rev. Lett. **56**, 2415 (1986); Phys. Rev. B **37**, 10159 (1988); N. Hamada, M. Hwang, and A. J. Freeman, *ibid*. **41**, 3620 (1990); M. Rohlfing, P. Krüger, and J. Pollman, *ibid*. **48**, 17791 (1993).
[27] E. L. Shirley, X. Zhu, and S. G. Louie, Phys. Rev. Lett. **69**, 2955 (1992), and unpublished.
[28] *Numerical Data and Functional Relationships in Science and Technology*, edited by K. H. Hellwege, Landolt-Börnstein, New Series, Group III, Vol. 7, Pt. a (Springer, New York, 1973).
[29] D. M. Ceperley and B. J. Alder, Phys. Rev. Lett. **45**, 566 (1980); we use the parametrization given by J. P. Perdew and A. Zunger, Phys. Rev. B **23**, 5048 (1981).
[30] D. R. Hamann, M. Schlüter, and C. Chiang, Phys. Rev. Lett. **43**, 1494 (1979).
[31] D. Vanderbilt, Phys. Rev. B **32**, 8412 (1985).
[32] E. L. Shirley and R. M. Martin, Phys. Rev. B **47**, 15 413 (1993).
[33] W. Müller, J. Flesch, and W. Meyer, J. Chem. Phys. **80**, 3297 (1984); W. Müller and W. Meyer, *ibid*. **80**, 3311 (1984).
[34] G. H. Jeung, J. P. Malrieu, and J. P. Daudey, J. Chem. Phys. **77**, 3571 (1982); P. A. Christiansen, Chem. Phys. Lett. **127**, 50 (1986); M. Krauss and W. J. Stevens, J. Chem. Phys. **93**, 4236 (1990), and references therein.
[35] L. Kleinman and D. M. Bylander, Phys. Rev. Lett. **48**, 1425 (1982).
[36] D. J. Chadi and M. L. Cohen, Phys. Rev. B **8**, 5747 (1973); H. J. Monkhorst and J. D. Pack, *ibid*. **13**, 5188 (1976).
[37] M. P. Teter, M. C. Payne, and D. C. Allan, Phys. Rev. B **40**, 12 255 (1989).
[38] C. G. Broyden, Math. Comput. **19**, 577 (1965).
[39] *CRC Handbook of Chemistry and Physics*, 75th ed. edited by D. R. Lide (Chemical Rubber, Ann Arbor, 1994).
[40] S. G. Louie, S. F. Froyen, and M. L. Cohen, Phys. Rev. B **26**, 1738 (1982).
[41] L. H. Yang (private communication).
[42] M. P. Surh (private communication).
[43] M. Methfessel, Phys. Rev. B **38**, 1537 (1988); M. Methfessel, C. O. Rodriguez, and O. K. Andersen, *ibid*. **40**, 2009 (1989).
[44] E. L. Shirley and S. G. Louie, Phys. Rev. Lett. **71**, 133 (1993); S. G. Louie and E. L. Shirley, J. Phys. Chem. Solids **54**, 1767 (1993).
[45] This is discussed in the work by Hybertsen and Louie (Ref. 14).
[46] J. E. Northrup, M. S. Hybertsen, and S. G. Louie, Phys. Rev. Lett. **59**, 7 (1987); Phys. Rev. B **39**, 8198 (1989); M. P. Surh, J. E. Northrup, and S. G. Louie, *ibid*. **38**, 5976 (1988).
[47] L. J. Terminello, J. J. Barton, and D. A. Lapiano-Smith, Phys. Rev. Lett. **70**, 599 (1993), and references therein.
[48] M. A. Van Hove, W. H. Weinberg, and C. M. Chan, *Low-Energy Electron Diffraction* (Springer, New York, 1986).
[49] See, for instance, J. A. Carlisle, T. Miller, and T. C. Chiang, Phys. Rev. B **49**, 13 600 (1994); J. A. Carlisle, M. T. Sieger, T. Miller, and T. C. Chiang, Phys. Rev. Lett. **71**, 2955 (1993).
[50] This is provided, for example, on p. 117 of Ref. 48.
[51] The generalization to arbitrary sign of ϵ would represent only a modest extension of the present work. Its need would arise when including high-order surface umklapp effects, which we, however, do not include in this work.
[52] For a review on angle-resolved photoemission, see F. J. Himpsel, Adv. Phys. **32**, 1 (1983).
[53] J. W. Gadzuk, Phys. Rev. B **10**, 5030 (1974); F. R. McFeely, J. Stöhr, G. Apai, P. S. Wehner, and D. A. Shirley, *ibid*. **14**, 3273 (1976).
[54] We use the same notation as in Michael Tinkham, *Group Theory and Quantum Mechanics* (McGraw-Hill, New York, 1964).
[55] For instance, see J. K. Taylor, *Statistical Techniques for Data Analysis* (Lewis, Chelsea, MI, 1990).